ARMA/USRMS 06-978

Stress Rate Dependent Strength of a Welded Tuff in Triaxial Tests

Ma, L.
Vector Engineering, Inc., Grass Valley, CA 95945, USA
Zhao, G.
School of Civil Engineering, Jinan University, P.R.China
Sunkara, A. and Daemen, J. J. K.
Department of Mining Engineering, University of Nevada, USA

ABSTRACT: Twenty seven triaxial compression tests have been conducted on welded tuff at constant and controlled axial piston displacement rates. The piston displacement rates were then converted to axial stress rates according to a nearly linear load-displacement relation. Specimens were tested in three orders of displacement rates or stress rates and at three confining pressures. Results of thirty eight uniaxial compression tests were incorporated into the group of triaxial tests. The specimens for the uniaxial tests were collected from the same location in Yucca Mountain as for the triaxial tests. The stress rates for triaxial and uniaxial tests are the same.

Strain gages were used for thirteen triaxial tests and all the uniaixal tests. Tests in three stress rates of the order of 0.4, 0.04 and 0.004 MPa/s and four confining pressures, 0, 5, 10 and 20 MPa were analyzed. Differential axial stress at failure increases with confining pressure and stress rate, both relations following power laws. Volumetric strain increases with confining pressure following an exponential law and decreases with stress rate following a power law. Young's modulus decreases with confining pressure and increases with stress rate. Poisson's ratio increases with confining pressure and stress rate.

1. INTRODUCTION

Results of twenty seven triaxial and thirty eight uniaxial compression tests on welded Topopah Spring tuff are presented. This testing program was a part of an investigation of long-term mechanical behavior of Yucca Mountain tuff in Nevada. Yucca Mountain has been selected as a candidate site for a High Level Nuclear Waste Repository in the United States [1]. The welded Topopah Spring Tuff is where the repository is to be excavated. Units exposed in the Topopah Spring Tuff include the Topopah Spring crystal-poor upper lithophysal zone (Tptpul), the Topopah Spring crystal-poor middle nonlithophysal zone (Tptpmn), the Topopah Spring crystal-poor lower lithophysal zone (Tptpll), and the Topopah Spring crystal-poor lower nonlithophysal zone (Tptpln) [2].

All the test specimens were from the Tptpmn zone. The specimens were prepared from rock drill cores received from the Sample Management Facility (SMF), Yucca Mountain Site Characterization Project. The drill cores were mainly from sidewalls of Alcove 5, which is for drift scale thermal test. The nominal diameter of the cores was 61 mm. For triaxial tests the ratio of length to diameter was controlled in the range of 1.9-2.5 to fit the 61 mm inner diameter Hoek triaxial cell. For uniaxial testing the ratio was between 1.8-2.6.

The triaxial tests were conducted at constant and controlled axial piston displacement rates. The piston displacement rates were then converted to axial stress rates according to a nearly linear load-displacement relation. Specimens were tested at three orders of displacement rates or stress rates and three confining pressures. Results of thirty eight uniaxial tests [3] were incorporated into the group of triaxial tests. The stress rates for triaxial and uniaxial tests are the same.

The average moisture content was 0.7%. The average density is 2.26 g/cm^3. The porosity of the

specimens in Tptpmn zone is in the range of 10-13% [3].

2. EXPERIMENTAL SETUP AND RESULTS

The tests were conducted in an MTS (Material Testing System), servo-controlled hydraulic test system. Load was measured using a load cell. Axial displacement was measured using an LVDT (Linear Variable Differential Transducer) in the MTS. Confining pressure was applied using an MTS servo-controlled hydraulic confining pressure generator which is controlled by the same program as axial load. The confining pressure is applied in such a way that the rate is slightly lower than axial loading rate to meet ASTM 2664 [4]. Strain was measured using electrical resistance strain gages. Four strain gages were used on each specimen for triaxial and six for uniaxial testing. Two or four measure axial strain. Two measure lateral strain. Strain gages were cemented at about midheight of each specimen. Strain in each direction was calculated by averaging all measurements in that direction. Strain gages were used in thirteen triaxial tests and all the uniaxial tests. The triaxial tests were conducted at three confining pressures, 5, 10 and 20 MPa and three stress rates of the order of 0.4, 0.04 and 0.004 MPa/s. Thus tests at four confining pressures and three stress rates are analyzed in this paper. Figure 1 shows a specimen with strain gage wires and the Hoek triaxial cell sitting in the MTS frame.

(a) (b)

Fig. 1. A specimen with strain gages and wires (a), and the Hoek triaxial cell sitting in the MTS frame (b).

Figures 2-5 give curves of differential axial stress (axial stress for uniaxial test)-axial strain (right), curves of differential axial stress-lateral strain (left) and curves of differential axial stress-volumetric strain (middle) for confining pressures 0, 5, 10 and 20 MPa, respectively at different stress rates. Test results used in the following analysis are summarized in Table 1. Volumetric strain is calculated by

$$\varepsilon_v = \varepsilon_1 + 2\varepsilon_3 \qquad (1)$$

where ε_1 is axial strain taken positive and ε_3 lateral strain taken negative.

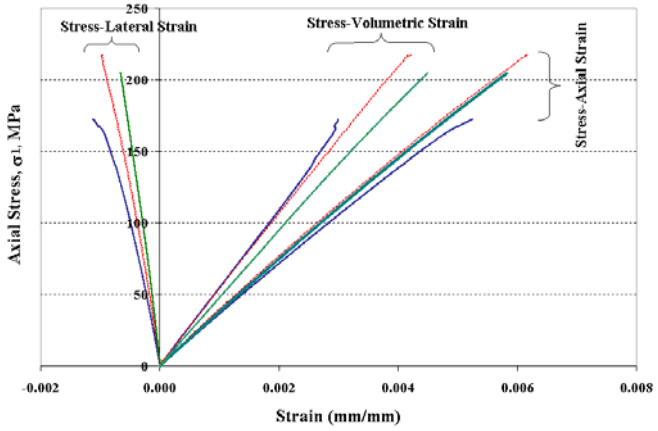

Fig. 2. Stress-strain curves for uniaxial compression tests. Specimen 01023657-3-U: axial stress at failure = 217 MPa, stress rate = 0.3604 MPa/s; Specimen 01023580-U: axial stress at failure = 172 MPa, stress rate = 0.0362 MPa/s; Specimen 01023662-1-U: axial stress at failure = 205 MPa, stress rate = 0.0036 MPa/s.

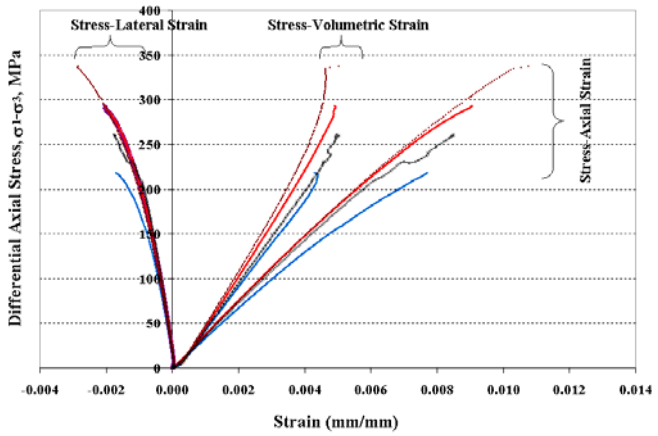

Fig. 3. Stress-strain curves for tests at confining pressure equal to 5 MPa. Specimen 01026153-1-T: axial stress at failure = 337 MPa, stress rate = 0.3772 MPa/s; Specimen 01026226-1-T: axial stress at failure = 262 MPa, stress rate = 0.3647 MPa/s; Specimen 01026258-4-T: axial stress at failure = 293 MPa, stress rate = 0.0038 MPa/s; Specimen 01026241-1-T: axial stress at failure = 218 MPa, stress rate = 0.0035 MPa/s.

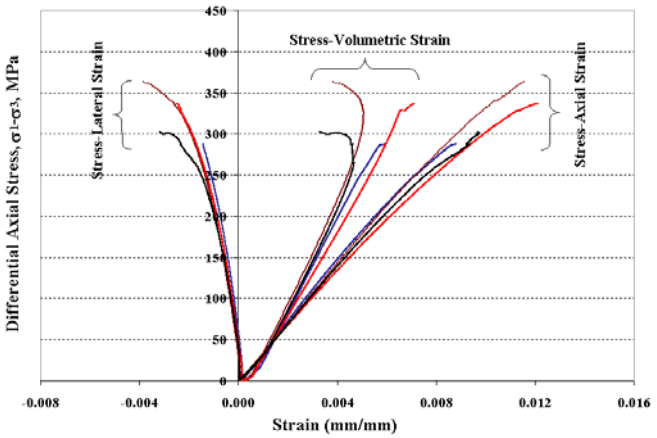

Fig. 4. Stress-strain curves for tests at confining pressure equal to 10 MPa. Specimen 01026144-1-T: axial stress at failure = 363 MPa, stress rate = 0.3743 MPa/s; Specimen 01026227-2-T: axial stress at failure = 303 MPa, stress rate = 0.0396 MPa/s; Specimen 01026225-6-T: axial stress at failure = 336 MPa, stress rate = 0.0375 MPa/s; Specimen 01026145-1-T: axial stress at failure = 288 MPa, stress rate = 0.0037 MPa/s.

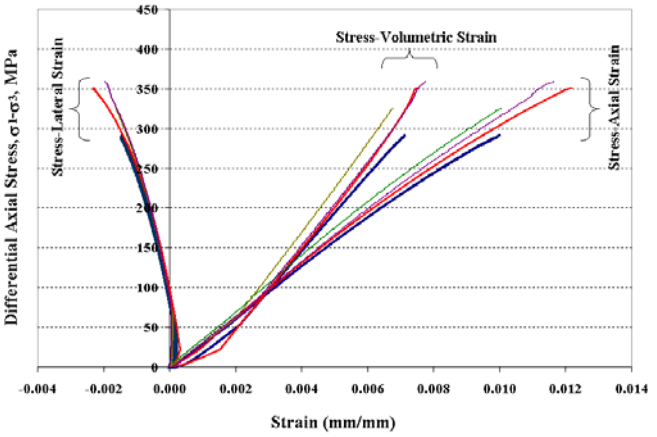

Fig. 5. Stress-strain curves for tests at confining pressure equal to 20 MPa. Specimen 01026145-2-T: axial stress at failure = 325 MPa, stress rate = 0.3952 MPa/s; Specimen 01026229-2-T: axial stress at failure = 358 MPa, stress rate = 0.3872 MPa/s; Specimen 01026255-1-T: axial stress at failure = 351 MPa, stress rate = 0.0036 MPa/s; Specimen 01026146-1-T: axial stress at failure = 292 MPa, stress rate = 0.0035 MPa/s.

3. ANALYSIS AND DISCUSSION

3.1. General observations

All the specimens in uniaxial tests exhibited brittle failure at all stress rates. The brittleness decreases with an increase of confining pressure. In uniaxial tests fractures were nearly parallel to the axis of the specimens, which failed predominantly by longitudinal splitting (Figure 6a). The main mechanism of inelastic deformation in brittle rocks under uniaxial compression is the development of cracks parallel to the compressive stress direction [5, 6]. In triaxial tests the main fracture exhibits inclined shear failure (Figure 6b). The inclination angle (to axis of specimen) increases with an increase of confining pressure. Stress-strain curves for uniaxial tests remain linear until very close to the peak (Figure 2). Nonlinearity increases with increasing confining pressure (Figures 3-5).

(a) (b)

Fig. 6. Specimens after failure: (a) After uniaxial test, longitudinal splitting dominates the failure mode. Specimen ID: 01023657-1-U (stress rate = 0.3805 MPa/s); (b) After triaxial test, shear failure. Specimen ID: 01026241-1-T (stress rate = 0.0035 MPa/s, confining pressure = 5 MPa).

3.2. Stress rate dependence of volumetric strain at failure

Given each stress rate and each confining pressure, volumetric strain at failure versus confining pressure and versus stress rate are plotted in Figures 7 and 8, respectively. To investigate the combined effects of confining pressure and stress rate on volumetric strain at failure, multivariate regression is performed. Eq. (2) is the regression equation that best describes the relationship among them.

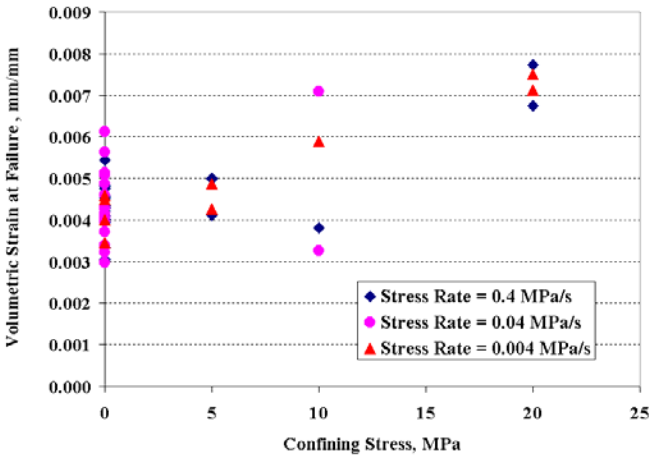

Fig. 7. Volumetric strain at failure as a function of confining pressure for each stress rate.

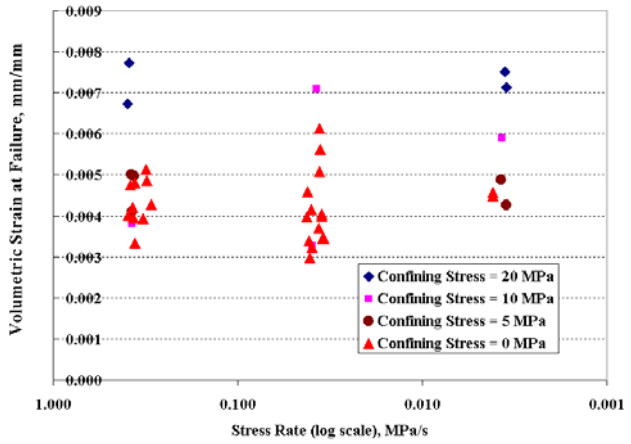

Fig. 8. Volumetric strain at failure as a function of stress rate for each confining pressure.

$$\varepsilon_v = 0.00417 e^{0.0259\,\sigma_3}\,\dot{\sigma}^{-0.00342} \qquad (2)$$

where $\dot{\sigma}$ denotes stress rate. In Eq. (2), volumetric strain at failure increases with an increase of confining pressure in an exponential law and decreases slightly with an increase of stress rate following a power law.

Eq. (2) was estimated using nonlinear regression. The results of the tests with strain measurement in Table 1 were used in the estimation. This regression was conducted using PROC NLIN with Marquardt algorithm in SAS (Version 8.2) program [7]. The PROC NLIN is a procedure to find least squares estimates of coefficients for nonlinear models. The Marquardt algorithm is a direct numerical search method.

In Eq. (2) student t-tests indicate that the coefficient of the whole term in the right hand side and the coefficient of σ_3 are significantly different from zero at the 95% confidence level (both P-values < 0.0001), the exponent of $\dot{\sigma}$ is not (P-value = 0.8, greater than 0.05). Pseudo-R-square for Eq. (2) is 0.52. This value explains the proportion of variance accounted for in the dependent variable by the model. It is equivalent to the R-square, the coefficient of determination, in linear regression.

Brittle failure of the tuff results from crack development [3]. Crack development causes dilatancy [6]. Dilatancy is an inelastic increase in volume due to fracturing. With an increase of confining pressure, more restriction is applied to decrease the dilatancy of a specimen. For a given confining pressure, the longer a specimen takes to fail, the more fatigue crack development and propagation will be created in the specimen. Dilatancy therefore gets larger.

3.3. *Stress Rate dependence of Young's modulus and Poisson's ratio*

Figures 9 and 10 give a plot of Young's modulus versus stress rate and a plot of Poisson's ratio versus stress rate at each confining stress level. Young's modulus and Poisson's ratio were calculated according to ASTM 3148 [8]. Eqs. (3) and (4) are the best estimates of their relations. The equations were estimated using the same method as in section 3.2.

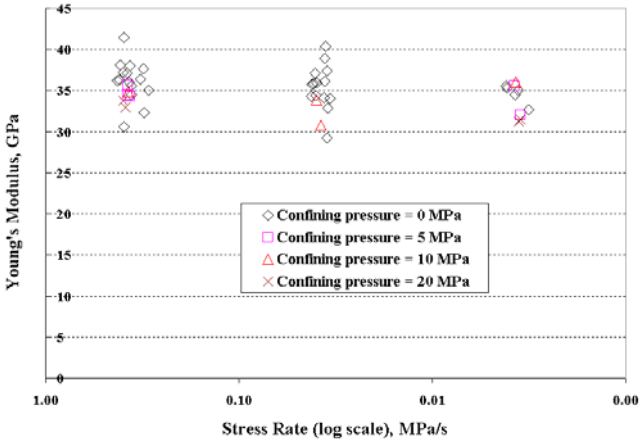

Fig. 9. Young's modulus as a function of stress rate for four confining pressures.

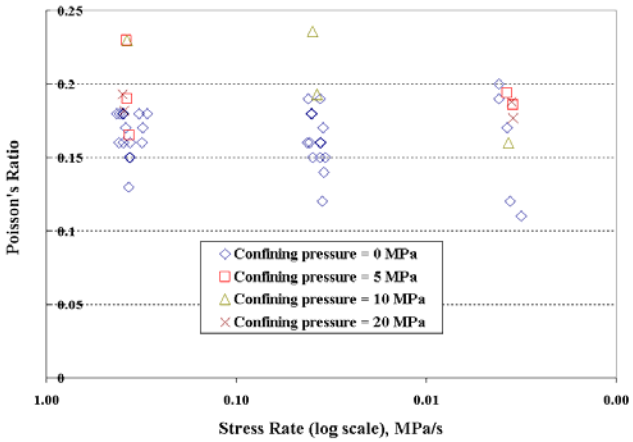

Fig. 10. Poisson's Ratio as a function of stress rate for four confining pressures.

$$E = 36.41 e^{-0.00462\,\sigma_3}\,\dot{\sigma}^{0.0084} \qquad (3)$$

$$\nu = 0.173 e^{0.00973\,\sigma_3}\,\dot{\sigma}^{0.0143} \qquad (4)$$

In Eq. (3) the 36.41 factor on the right hand side (P value < 0.0001) and the coefficient of σ_3 (P-value = 0.0073) are significantly different from zero at the 95% confidence level, the exponent of $\dot{\sigma}$ is not (P-

value = 0.11, greater than 0.05). Pseudo-R-square is 0.22.

Young's modulus decreases with an increase in confining pressure, and increases slightly with an increase in stress rate. The former is the opposite from the observation by Li et al. [9] for the Bukit Timah granite of Singapore. They reported that Young's modulus seems to increase slightly with increasing confining pressure.

From Eq. (4), Poisson's ratio increases with confining pressure and increases slightly with stress rate. The coefficient of the whole term in the right hand side (P value < 0.0001) and the coefficient of σ_3 (P-value = 0.0033) are significantly different from zero at the 95% confidence level, the exponent of $\dot{\sigma}$ is not (P-value = 0.22, greater than 0.05). Pseudo-R-square is 0.19.

3.4. *Stress rate dependency of differential axial stress at failure*

Differential axial stress at failure increases with confining pressure and stress rate as shown in Figures 11 and 12. The brittle strength increases at higher confining pressure, because it becomes more difficult for microcracks to open and propagate. The dependency of differential axial stress on stress rate and confining stress can be best described by a power law (e.g. [10, 11, 12]) as in Eq. (5). Eq. (5) is the best estimation for the test results. When $\dot{\sigma}$ = 1, Eq. (5) is an expression of the relation between differential axial stress at failure and confining pressure at standard loading rate specified in ASTM 2938 [13]. If σ_3 = 0, Eq. (5) reduces to the case of stress rate dependency under uniaxial compression. The intercept in the parenthesis is the average uniaxial strength of the tuff at standard loading rate.

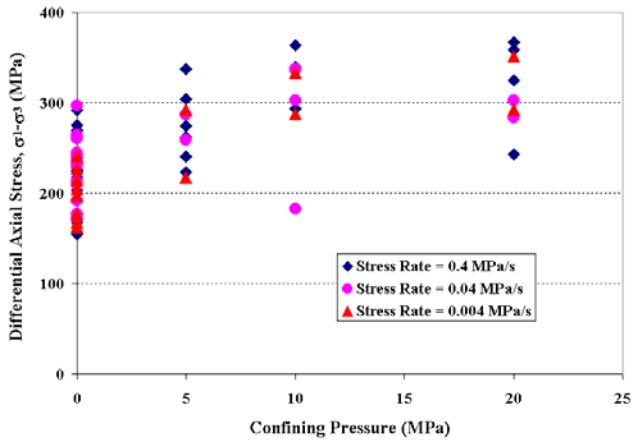

Fig. 11. Differential axial stress as a function of confining pressure for each stress rate.

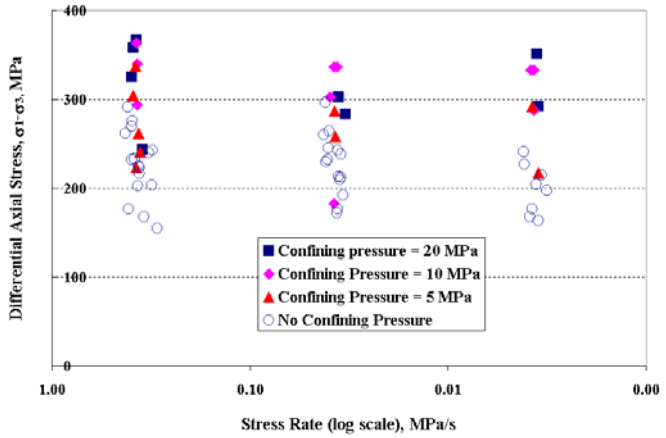

Fig. 12. Differential axial stress as a function of stress rate for each confining pressure.

$$\sigma_1 - \sigma_3 = (229.6 + 31.9\sigma_3^{0.4})\dot{\sigma}^{0.014} \qquad (5)$$

Eq. (5) was estimated using the same procedure described in sections 3.2 and 3.3. Student t-tests indicate that the coefficient and the exponent of σ_3 in Eq. (5) are significantly different from zero at the 95% confidence level (P-value = 0.05 for coefficient, P-value = 0.04 for exponent), but the exponent of $\dot{\sigma}$ is not (P-value = 0.2, greater than 0.05). Pseudo-R-square for Eq. (3) is 0.52. Figure 13 shows a 3-D plot of Eq. (5).

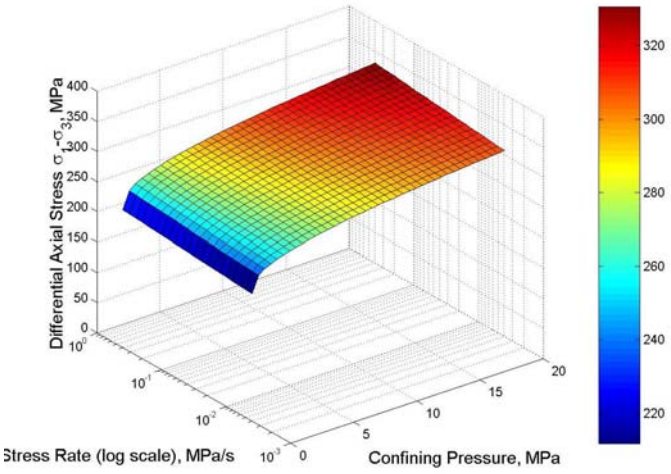

Fig. 13. Differential axial stress as a function of confining pressure and stress rate.

4. CONCLUSIONS

- Brittle failure was observed in uniaxial compression tests at all stress rates.
- Volumetric strain at failure increases with an increase of confining pressure following an exponential law and decreases slightly with an

increase in stress rate according to a power law.

- Young's modulus decreases with an increase in confining pressure following an exponential law and increases slightly with an increase of stress rate following a power law.
- Poisson's ratio increases with confining pressure following an exponential law and increases slightly with stress rate following a power law.
- Differential axial stress at failure increases with confining pressure and stress rate according to a power law.
- These conclusions have to be tempered and qualified by the fact that the data set is small, the rock properties are highly variable, and hence the resulting statistical significance is marginal, at best.

ACKNOWLEDGEMENTS

We thank mr. Jaime gonzalez, doe contract manager and mr. Rick blitz for experimental work.

This paper was prepared by university of nevada reno pursuant to a cooperative agreement fully funded by the united states department of energy, and neither university and community college system of nevada nor any of its contractors or subcontractors nor the united states department of energy, nor any person acting on behalf of either:

Makes any warranty or representation, express or implied, with respect to the accuracy, completeness, or usefulness of the information contained in this report, or that the use of any information, apparatus, method, or process disclosed in this report may not infringe privately-owned rights; or

Assumes any liabilities with respect to the use of, or for damages resulting from the use of, any information, apparatus, method or process disclosed in this report. Reference herein to any specific commercial product, process, or service by trade name, trademark, manufacturer, or otherwise, does not necessarily constitute or imply its endorsement, recommendation, or favoring by the united states department of energy. The views and opinions of authors expressed herein do not necessarily state or reflect those of the united states department of energy.

REFERENCES

1. OCRWM (Office of Civilian Radioactive Waste Management). Website: http://www.ocrwm.doe.gov, September 2004.
2. OCRWM. 1999. *Geology of the ECRB Cross Drift-Exploratory Studies Facility, Yucca Mountain Project, Yucca Mountain, Nevada*, Bureau of Reclamation and U.S. Geological Survey, Denver, Colorado.
3. Ma, L. and J.J.K. Daemen. 2006. Strain Rate Dependent Strength and Stress-Strain Characteristics of a Welded Tuff. *Bull. Eng. Geol.Env.*, http://dx.doi.org/10.1007/s10064-005-0038-6.
4. ASTM D 2664 Standard Test Method for Triaxial Compressive Strength of Undrained Rock Core Specimens without Pore Pressure Measurements. In *Annual Book of ASTM Standards, Section 4, Construction*. Volume 04.08 Soil and Rock; Building Stones. American Society for Testing and Materials, Philadelphia.
5. Walsh, J. B. 1965. The Effect of Cracks on the Uniaxial Elastic Compression of Rocks. *J. Geophys. Res*. 70: 2, 399-411.
6. Brace, W. F., B.W. Paulding, Jr., and C.H. Scholz. 1966. Dilatancy in the Fracture of Crystalline Rocks. *J. Geophys. Res*. 71: 16, 3,939-3,953.
7. Fernandez G. 2003. *Data Mining Using SAS Applications.* Chapman & Hall/CRC.
8. ASTM D 3148, Standard Test Method for Elastic Moduli of Intact Rock Core Specimens in Uniaxial Compression. In *Annual Book of ASTM Standards, Section 4, Construction*. Volume 04.08 Soil and Rock; Building Stones. American Society for Testing and Materials, Philadelphia.
9. Li, H.B., J. Zhao and T.J. Li. 1999. Triaxial Compression Tests on a Granite at Different Strain Rates and Confining Pressures. *Int. J. Rock Mech. Min. Sci.*, Technical Note. 30, 1057-1063.
10. Bieniawski, Z.T. 1974. Establishing the Strength of Rock Mechanics, J. South African Inst. Min. Metallugy. 74, 312-320.
11. Goodman, R. E. 1980. *Introduction to Rock Mechanics*. John Wiley & Sons, New York, p.88.
12. Brady, B.H.G. and E.T. Brown. 1985. *Rock Mechanics for Underground Mining*, George Allen & Unwin, London, p110.
13. ASTM D 2938, Standard Test Method for Unconfined Compressive Strength of Intact Rock Core Specimens. In *Annual Book of ASTM Standards, Section 4, Construction*. Volume 04.08 Soil and Rock; Building Stones. American Society for Testing and Materials, Philadelphia.

Table 1. Summary of triaxial and uniaxial compression test results

Serial #	Specimen ID	σ_3, MPa	$\dot{\sigma}$, MPa/s	σ_1, MPa	E, GPa	ν	ε_v,mm/mm
1	01026149-1-T	10	0.3709	349.65	NA	NA	NA
2	01026154-1-T	5	0.3589	245.59	NA	NA	NA
3	01026155-4-T	5	0.3882	309.54	NA	NA	NA
4	01026157-3-T	5	0.0372	291.97	NA	NA	NA
5	01026158-2-T	10	0.0037	342.99	NA	NA	NA
6	01026160-1-T	20	0.3741	386.53	NA	NA	NA
7	01026160-2-T	10	0.3727	303.57	NA	NA	NA
8	01026237-T	10	0.0378	192.32	NA	NA	NA
9	01026246-1-T	10	0.0038	343.18	NA	NA	NA
10	01026248-4-T	20	0.3492	263.32	NA	NA	NA
11	01026250-2-T	10	0.0365	346.93	NA	NA	NA
12	01026257-1-T	20	0.0359	322.84	NA	NA	NA
13	01026259-1-T	5	0.0371	263.58	NA	NA	NA
14	01026543-1-T	20	0.0330	303.15	NA	NA	NA
15	01026241-1-T	5	0.0035	222.67	32.06	0.19	0.0043
16	01026145-1-T	10	0.0037	297.62	36.01	0.16	0.0059
17	01026146-1-T	20	0.0035	312.23	31.55	0.18	0.0071
18	01026255-1-T	20	0.0036	370.88	31.20	0.19	0.0075
19	01026258-4-T	5	0.0038	297.54	35.60	0.19	0.0049
20	01026153-1-T	5	0.3772	342.13	34.40	0.23	0.0050
21	01026144-1-T	10	0.3743	373.76	34.89	0.23	0.0038
22	01026145-2-T	20	0.3952	344.98	33.77	0.19	0.0067
23	01026541-2-T	5	0.3748	228.3	35.64	0.19	0.0041
24	01026225-6-T	10	0.0375	346.46	30.74	0.19	0.0071
25	01026227-2-T	10	0.0396	312.55	33.88	0.24	0.0033
26	01026226-1-T	5	0.3647	266.74	34.33	0.17	0.0050
27	01026229-2-T	20	0.3872	378.43	33.00	0.18	0.0077
28	01023580-U	0	0.0362	172.00	34.10	0.19	0.0030
29	01023660-1-U	0	0.0039	168.10	33.08	NA	NA
30	01023657-1-U	0	0.3805	233.16	37.14	0.17	0.0041
31	01023697-1-U	0	0.0034	215.19	31.85	NA	NA
32	01023697-4-U	0	0.0035	163.16	29.95	NA	NA
33	01023657-3-U	0	0.3604	216.95	35.58	0.16	0.0042
34	01023662-2-U	0	0.3129	203.36	37.64	0.16	0.0033
35	01023664-U	0	0.3238	239.62	36.39	0.18	0.0040
36	01023701-1-U	0	0.3094	242.89	32.36	0.17	0.0048
37	01023687-1-U	0	0.3921	275.22	41.43	0.16	0.0045
38	01023740-1-U	0	0.3655	225.33	38.02	0.15	0.0040
39	01025224-3-U	0	0.2939	154.49	35.03	0.18	0.0039
40	01025230-2-U	0	0.3951	269.62	37.19	0.18	0.0043
41	01023667-1-U	0	0.0361	176.63	38.96	0.15	0.0032
42	01025259-1-U	0	0.0349	238.26	37.43	0.17	0.0051
43	01025230-1-U	0	0.0352	209.46	29.28	0.12	0.0061
44	01023722-2-U	0	0.0417	296.47	35.75	0.19	0.0049
45	01025235-2-U	0	0.0412	229.75	35.87	0.16	0.0043
46	01023687-2-U	0	0.0357	213.02	40.36	0.16	0.0037
47	01023686-2-U	0	0.0361	242.43	36.16	0.16	0.0041
48	01023695-2-U	0	0.3691	203.02	36.00	0.13	0.0043
49	01025234-1-U	0	0.4137	291.64	36.32	0.16	0.0054
50	01023702-2-U	0	0.3611	223.90	34.48	0.15	0.0048

Table 1 Continued

51	01023691-1-U	0	0.0423	259.94	34.35	0.16	0.0051
52	01023707-1-U	0	0.0339	192.01	34.07	0.15	0.0040
53	01023686-1-U	0	0.0405	232.54	37.12	0.18	0.0040
54	01025260-1-U	0	0.0346	212.17	32.86	0.14	0.0056
55	01023694-2-U	0	0.0401	244.80	34.44	0.18	0.0046
56	01023662-1-U	0	0.0036	204.55	35.04	0.12	0.0045
57	01025226-1-U	0	0.0041	227.37	35.32	0.20	0.0034
58	01023657-4-U	0	0.4254	261.63	36.18	0.18	0.0046
59	01023687-3-U	0	0.0041	241.02	35.58	0.19	0.0040
60	01023707-3-U	0	0.3942	232.55	30.56	0.18	0.0043
61	01023743-1-U	0	0.3418	167.47	37.59	NA	NA
62	01023747-1-U	0	0.0397	264.26	35.91	0.15	0.0034
63	01023750-U	0	0.4105	176.52	38.10	0.18	0.0030
64	01023751-1-U	0	0.0037	176.95	34.51	0.17	0.0034
65	01025233-1-U	0	0.0032	197.48	32.73	0.11	0.0046
Note: NA - Not Available.							